


Electromagnetically induced transparency, absorption, and microwave-field sensing in a Rb vapor cell with a three-color all-infrared laser system

N. Thaicharoen,^{1,*} K. R. Moore,^{1,†} D. A. Anderson,² R. C. Powel,^{1,‡} E. Peterson,^{1,§} and G. Raithel^{1,2}

¹*Department of Physics, University of Michigan, Ann Arbor, Michigan 48109, USA*

²*Rydberg Technologies, Inc., Ann Arbor, Michigan 48104, USA*

 (Received 23 May 2019; revised manuscript received 19 November 2019; published 26 December 2019)

A comprehensive study of three-photon electromagnetically induced transparency (EIT) and absorption (EIA) on the rubidium cascade $5S_{1/2} \rightarrow 5P_{3/2}$ (laser wavelength 780 nm), $5P_{3/2} \rightarrow 5D_{5/2}$ (776 nm), and $5D_{5/2} \rightarrow 28F_{7/2}$ (1260 nm) is performed. The 780-nm probe and 776-nm dressing beams are counteraligned through a Rb room-temperature vapor cell, and the 1260-nm coupler beam is co- or counteraligned with the probe beam. Several cases of EIT and EIA, measured over a range of detunings of the 776-nm beam, are studied. The observed phenomena are modeled by numerically solving the Lindblad equation, and the results are interpreted in terms of the probe-beam absorption behavior of velocity- and detuning-dependent dressed states. Interaction-time effects are discussed. To explore the utility of three-photon Rydberg EIA and EIT for microwave electric-field diagnostics, a sub-THz field generated by a signal source and a frequency quadrupler is applied to the Rb cell. The 100.633-GHz field resonantly drives the $28F_{7/2} \leftrightarrow 29D_{5/2}$ transition and causes Autler-Townes splittings in the Rydberg EIA and EIT spectra, which are measured and employed to characterize the performance of the microwave quadrupler.

DOI: [10.1103/PhysRevA.100.063427](https://doi.org/10.1103/PhysRevA.100.063427)

I. INTRODUCTION

Rydberg levels of atoms and molecules are characterized by a tenuously bound valence electron the marginal atomic binding of which leads to high susceptibilities to external fields and other perturbations [1]. Electric dipole transitions between Rydberg states are in the microwave and sub-THz range, with electric dipole matrix elements scaling as the square of the principal quantum number n . Hence, Rydberg atoms exhibit a strong response to applied dc and radio-frequency (rf) electric fields. Based on these properties, Rydberg atoms are now being used and proposed widely in atomic measurement standards for electric fields [2–9] and in Rydberg-atom-based communications [10–12], with cell-internal structures providing enhanced sensitivity [13]. In the employed method of Rydberg electromagnetically induced transparency (EIT) [14,15], a coupling laser resonantly couples a low-lying intermediate level, $|e\rangle$, to one or more Rydberg levels, $|r_i\rangle$, thereby inducing EIT [16,17] for a probe beam that measures absorption on the transition between $|g\rangle$ and $|e\rangle$. Rydberg interactions in cold-atom Rydberg-EIT have been measured [18,19] and

theoretically investigated [20,21]. In the present paper in room-temperature vapor cells, the observed Rydberg-EIT spectra serve as an optical probe for the energy levels of the Rydberg states $|r_i\rangle$, as well as for their energy-level shifts in applied dc and rf electric fields. Owing to the simplicity of vapor-cell spectroscopy, Rydberg-EIT-based atomic field measurement in room-temperature cesium and rubidium vapor cells is particularly attractive for novel metrology approaches that harness the quantum-mechanical properties of atoms. Efforts are underway to develop the method into atom-based, calibration-free, sensitive field measurement and receiver instrumentation.

Since the matrix elements for optical Rydberg-atom excitation, $\langle r_i | \hat{\mathbf{r}} | e \rangle$, are quite small, two-color Rydberg-EIT as described above often requires expensive commercial lasers for the coupling transition. For instance, in Rb and Cs Rydberg-EIT one typically requires a coupling laser at respective wavelengths of 480 and 510 nm, ≈ 1 -MHz linewidth, tens of mW of power, and good spatial mode quality. There is an interest in replacing the two-color EIT with schemes involving three low-power infrared lasers instead [22–24].

In our paper, we compare experimental and theoretical results in three-color EIT and electromagnetically induced absorption (EIA) in a Rb vapor cell. Several schemes with different relative propagation directions of the three optical beams and intermediate-transition detuning values are studied, and regimes suitable for three-photon EIT and EIA spectroscopy of Rydberg energy levels are identified. The results are discussed in context with related works. We further demonstrate the utility of the setup for characterizing a commercial sub-THz frequency quadrupling system. Numerical solutions of the Lindblad equation and an analytical

*Corresponding author: nithi@umich.edu; Present address: Faculty of Science, Chiang Mai University, Chiang Mai 50200, Thailand.

†Present address: SRI International 201 Washington Rd, Princeton, NJ 08540, USA.

‡Present address: Michigan State University, East Lansing, Michigan 48824, USA.

§Present address: Department of Physics, Harvard University, Cambridge, Massachusetts 02138, USA.

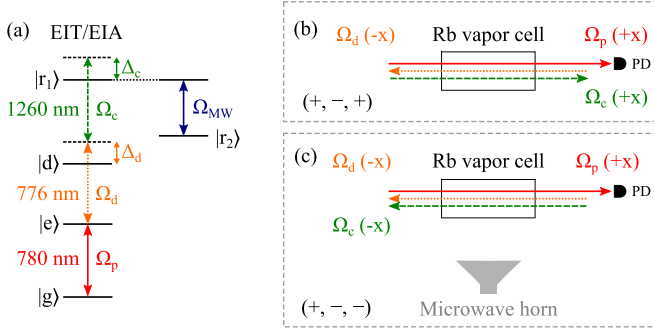


FIG. 1. (a) Energy-level diagram for the three-photon EIT experiment. (b, c) Experimental setup. The 780-nm beam counterpropagates with the 776-nm beam. The 1260-nm beam propagates either (b) in the same direction as the 780-nm beam or (c) in the opposite direction. The propagation-direction configurations for the 780-, 776-, and 1260-nm beams are denoted $(+, -, +)$ and $(+, -, -)$, respectively.

dressed-state approach are employed to model and interpret the data.

II. EXPERIMENTAL SETUP

The energy-level diagram of the experiment is shown in Fig. 1(a). Following the terminology in [23], the three transitions from the ground into the Rydberg levels are referred to as the probe, the dressing, and the coupler transitions. All laser sources are home-built external-cavity diode lasers. The 780-nm probe laser is locked to the $|g\rangle(5S_{1/2}, F=3) \rightarrow |e\rangle(5P_{3/2}, F'=4)$ transition at zero atomic velocity. Part of the locked 780-nm beam is sent into another rubidium reference vapor cell and counterpropagated with a small portion of the 776-nm laser to form a saturated spectroscopic signal to lock the 776-nm dressing laser, which is set at selected detunings Δ_d from the $|e\rangle \rightarrow |d\rangle(5D_{5/2})$ transition at zero velocity. (The $5D_{5/2}$ hyperfine levels were not resolved in the present setup). The 1260-nm coupling laser is scanned through the $|d\rangle \rightarrow |r_1\rangle(28F_{7/2})$ transition. The offset frequency of the 1260-nm laser, Δ_c , is calibrated by recording the transmission of a small fraction of the 1260-nm beam through a Fabry-Pérot cavity with a free spectral range of 375 MHz. The power of the transmitted probe beam is measured with a photodiode as a function of Δ_c .

The 780-nm probe beam has a power of $P \lesssim 10 \mu\text{W}$ and a Gaussian beam-waist parameter w_0 of $\gtrsim 80 \mu\text{m}$, corresponding to a Rabi frequency $\Omega_p \lesssim 2\pi \times 22 \text{ MHz}$. For the 776-nm dressing beam, $P \lesssim 3 \text{ mW}$, $w_0 \gtrsim 140 \mu\text{m}$, and $\Omega_d \lesssim 2\pi \times 67 \text{ MHz}$, and for the 1260-nm coupling beam $P \lesssim 7 \text{ mW}$, $w_0 \gtrsim 75 \mu\text{m}$, and $\Omega_c \lesssim 2\pi \times 27 \text{ MHz}$. The listed Rabi frequencies are averages over the relevant magnetic transitions and are calculated for the respective beam centers. The actual effective Rabi frequencies are considerably lower due to averaging over the near-Gaussian spatial beam profiles, possible imperfections in the beam overlaps, and possible beam-size increases due to lensing in the walls of the vapor cell.

The three laser beams must be carefully aligned and overlapped within the $L = 7.5\text{-cm}$ -long Rb vapor cell. The first alignment step is to establish two-photon EIT by

counterpropagating the 780-nm probe with the 776-nm dressing beam. This couples the lower three levels, $|g\rangle \leftrightarrow |e\rangle \leftrightarrow |d\rangle$. We optimize the $5D_{5/2}$ EIT signal by fine adjusting the overlap between the probe and dressing beams and adjusting the power of the 780-nm probe beam. Then, we apply the 1260-nm coupler beam either in the same direction as the 780-nm probe beam $[(+, -, +)$ configuration, see Fig. 1(b)] or in the direction opposite to the 780-nm beam $[(+, -, -)$ configuration, see Fig. 1(c)]. We fix the frequency of the 780-nm probe and the 776-nm dressing beams while scanning Δ_c . The EIA or EIT signals are observed on top of the $5D_{5/2}$ -EIT background.

To show the utility of three-photon EIT and EIA in probing microwave and sub-THz electric fields, we have calibrated the electric-field strength of a 100-GHz transmission system. A microwave source supplies a 25-GHz signal to an active quadrupler, which feeds 100-GHz radiation to a standard-gain horn. The three-photon EIT and EIA field probe is placed in the far field of the horn, as indicated in Fig. 1(c). We test EIT and EIA schemes to calibrate the 100-GHz electric field against the 25-GHz power the signal generator supplies to the quadrupler.

III. NUMERICAL MODEL

A. Model outline

The system is modeled with the five-level system shown in Fig. 1(a). We numerically solve the Lindblad equation of the system and obtain steady-state solutions of the density matrix, $\hat{\rho}$. We ignore magnetic substructure, other than including m -averaged angular matrix elements in the calculation of the Rabi frequencies. We assume a closed decay scheme in which $|e\rangle$ decays at a rate of $\Gamma_e = 2\pi \times 6 \text{ MHz}$ into $|g\rangle$, $|d\rangle$ decays at a rate of $\Gamma_d = 2\pi \times 0.66 \text{ MHz}$ into $|e\rangle$, $|r_1\rangle$ decays at a rate of $\Gamma_{r1} = 2\pi \times 10 \text{ kHz}$ into $|d\rangle$, and $29D_{5/2}(|r_2\rangle)$ decays at a rate of $\Gamma_{r2} = 2\pi \times 10 \text{ kHz}$ into $|e\rangle$. The values of Γ_{r1} and Γ_{r2} are sufficiently small that they have no measurable effect in our paper. We neglect the (minor) decay of $5D_{5/2}(|d\rangle)$ into $6P_{3/2}$ and the decays of the Rydberg levels out of the five-level system. The system has four coherent-drive fields. The probe is linearly polarized in the horizontal direction, while all other fields are polarized vertically. The Rabi frequencies at the beam centers are calculated from the beam parameters provided above, the known radial electric dipole matrix elements for the various transitions, and an average of the angular matrix elements over the relevant magnetic transitions.

B. Formalism

For a given set of probe, dressing, coupler, and (optional) rf Rabi frequencies, Ω_p , Ω_d , Ω_c , and Ω_{rf} , and respective zero-velocity atom-field-detunings, Δ_p , Δ_d , Δ_c , and Δ_{rf} , we obtain the steady-state solution of the Lindblad equation in a four-color field picture. Since our probe Rabi frequencies are larger than the $5P_{3/2}(|e\rangle)$ decay rate, we do not make a weak-probe approximation. The atom-field detunings are defined as field frequencies minus atomic-transition frequencies. Accounting for the Doppler effect, the detunings $\Delta_{i,a}$ with $i = p, d, c$, and rf are, in the four-color field picture and in

the frame of reference that is co-moving with the atom,

$$\begin{aligned}\Delta_{p,a} &= \Delta_p - k_p v, \\ \Delta_{d,a} &= \Delta_d + k_d v, \\ \Delta_{c,a} &= \Delta_c \pm k_c v, \\ \Delta_{\text{rf},a} &= \Delta_{\text{rf}} - k_{\text{rf}} v,\end{aligned}\quad (1)$$

where v denotes the atom velocity along the probe-beam direction, the wave numbers k_i are defined as positives, and the term $\pm k_c$ corresponds with the $(+, -, \mp)$ configurations, respectively. The wave-vector component of the rf field in the direction of the laser beams, k_{rf} , is so small that it can be neglected. In the Lindblad equation

$$\dot{\hat{\rho}} = \frac{i}{\hbar}[\hat{\rho}, \hat{H}] + L(\hat{\rho}), \quad (2)$$

$$L(\hat{\rho}) = \begin{pmatrix} \Gamma_e \rho_{22} & -\frac{1}{2} \Gamma_e \rho_{12} & -\frac{1}{2} \Gamma_d \rho_{13} & -\frac{1}{2} \Gamma_{r1} \rho_{14} & -\frac{1}{2} \Gamma_{r2} \rho_{15} \\ -\frac{1}{2} \Gamma_e \rho_{21} & -\Gamma_e \rho_{22} + \Gamma_d \rho_{33} + \Gamma_{r2} \rho_{55} & -\frac{1}{2} (\Gamma_e + \Gamma_d) \rho_{23} & -\frac{1}{2} (\Gamma_e + \Gamma_{r1}) \rho_{24} & -\frac{1}{2} (\Gamma_e + \Gamma_{r2}) \rho_{25} \\ -\frac{1}{2} \Gamma_d \rho_{31} & -\frac{1}{2} (\Gamma_e + \Gamma_d) \rho_{32} & -\Gamma_d \rho_{33} + \Gamma_{r1} \rho_{44} & -\frac{1}{2} (\Gamma_d + \Gamma_{r1}) \rho_{34} & -\frac{1}{2} (\Gamma_d + \Gamma_{r2}) \rho_{35} \\ -\frac{1}{2} \Gamma_{r1} \rho_{41} & -\frac{1}{2} (\Gamma_e + \Gamma_{r1}) \rho_{42} & -\frac{1}{2} (\Gamma_d + \Gamma_{r1}) \rho_{43} & -\Gamma_{r1} \rho_{44} & -\frac{1}{2} (\Gamma_{r1} + \Gamma_{r2}) \rho_{45} \\ -\frac{1}{2} \Gamma_{r2} \rho_{51} & -\frac{1}{2} (\Gamma_e + \Gamma_{r2}) \rho_{52} & -\frac{1}{2} (\Gamma_d + \Gamma_{r2}) \rho_{53} & -\frac{1}{2} (\Gamma_{r1} + \Gamma_{r2}) \rho_{54} & -\Gamma_{r2} \rho_{55} \end{pmatrix}. \quad (4)$$

The steady-state solution for $\hat{\rho}$ yields the coherence ρ_{12} as a function of atom velocity v and all field-strength, field-detuning, and decay parameters. The absorption coefficient and the refractive index of the atomic vapor for the probe beam then follow:

$$\begin{aligned}\alpha &= \frac{\omega_p}{c} \frac{2n_V d_{eg}}{\epsilon_0 E_p} \int P(v) \text{Im}(\rho_{12}) dv, \\ (n-1) &= \frac{1}{2} \frac{2n_V d_{eg}}{\epsilon_0 E_p} \int P(v) \text{Re}(\rho_{12}) dv.\end{aligned}\quad (5)$$

Here, $\omega_p = k_p c$, n_V denotes the atom volume density, d_{eg} denotes the probe electric dipole matrix element, E_p denotes the probe-laser electric-field amplitude, and $P(v)$ denotes the normalized one-dimensional Maxwell velocity distribution in the room-temperature vapor cell. In the n_V value we account for the natural abundance of ^{85}Rb in our cell (72%) and the statistical weight of ^{85}Rb $F = 3$ (58.3%). For the probe electric dipole matrix element averaged over the magnetic transitions we use $d_{eg} = 1.9 \text{ ea}_0$, where ea_0 is the atomic unit of electric dipole moment. The transmission values plotted in Figs. 2(b), 3(d), 4(b), and 7 are given by $T(\Delta_c) = \exp(-\alpha L)$ with $L = 7.5 \text{ cm}$.

IV. THREE-PHOTON EIA AND EIT

A. $(+, -, -)$ configuration

1. Measurement and simulation results

The first objective of the paper is to identify beam directions, Rabi frequencies, and detunings that yield EIT and EIA signatures suitable to measure Rydberg energy-level positions and shifts. We find several regimes of robust EIA and EIT for the beam-propagation configurations $(+, -, \mp)$ defined in Fig. 1.

the Hamiltonian matrix is

$$H = \hbar \begin{pmatrix} -\Delta_1 & \Omega_p/2 & 0 & 0 & 0 \\ \Omega_p/2 & -\Delta_2 & \Omega_d/2 & 0 & 0 \\ 0 & \Omega_d/2 & -\Delta_3 & \Omega_c/2 & 0 \\ 0 & 0 & \Omega_c/2 & -\Delta_4 & \Omega_{\text{rf}}/2 \\ 0 & 0 & 0 & \Omega_{\text{rf}}/2 & -\Delta_5 \end{pmatrix}. \quad (3)$$

There, the Hamiltonian is expressed in the dressed-state basis $\{|1\rangle, \dots, |5\rangle\}$ that corresponds with the bare atomic states $\{|g\rangle, |e\rangle, |d\rangle, |r1\rangle, |r2\rangle\}$, in that order. The field-free dressed-state energies are $\Delta_1 = 0$, $\Delta_2 = \Delta_1 + \Delta_{p,a}$, $\Delta_3 = \Delta_2 + \Delta_{d,a}$, $\Delta_4 = \Delta_3 + \Delta_{c,a}$, and $\Delta_5 = \Delta_4 - \Delta_{\text{rf},a}$. The fifth state is not used when the rf field is off. For the Lindblad operator $L(\hat{\rho})$ we use the level decay rates given in Sec. III A, with no additional level dephasing terms:

The $(+, -, -)$ configuration has been studied in [23] for a case in cesium and $\Delta_d = 0$. The Rb case studied here differs from [23] in that the differential probe-dressing Doppler shift, $(k_d - k_p)v$, is near zero for a wide range of velocities within the Maxwell velocity distribution, because the probe and dressing wavelengths are nearly identical in the Rb case studied experimentally in this paper. This leads to a stronger

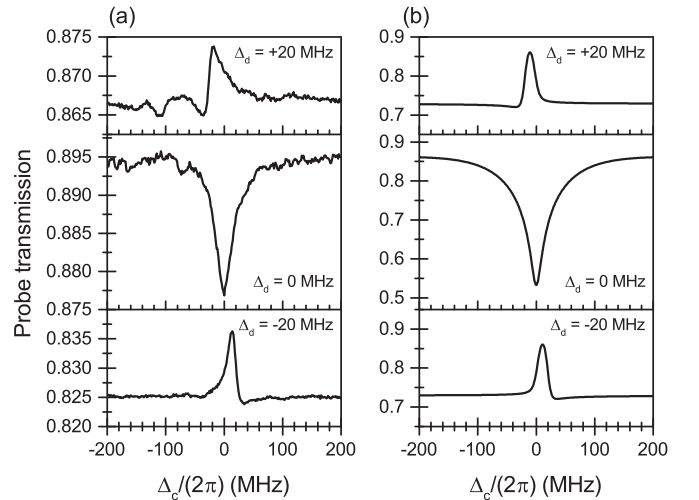


FIG. 2. (a) Change in experimental probe transmission vs coupler-laser detuning when the lasers are in $(+, -, -)$ configuration. Strong EIA is observed when $\Delta_d = 0$, and EIT is observed when $\Delta_d = \pm 2\pi \times 20 \text{ MHz}$. (b) Probe transmissions calculated with the model in Sec. III for cell temperature of 300 K, cell length $L = 7.5 \text{ cm}$, and with $\Omega_p = 2\pi \times 10 \text{ MHz}$, $\Omega_d = 2\pi \times 25 \text{ MHz}$, and $\Omega_c = 2\pi \times 18 \text{ MHz}$.

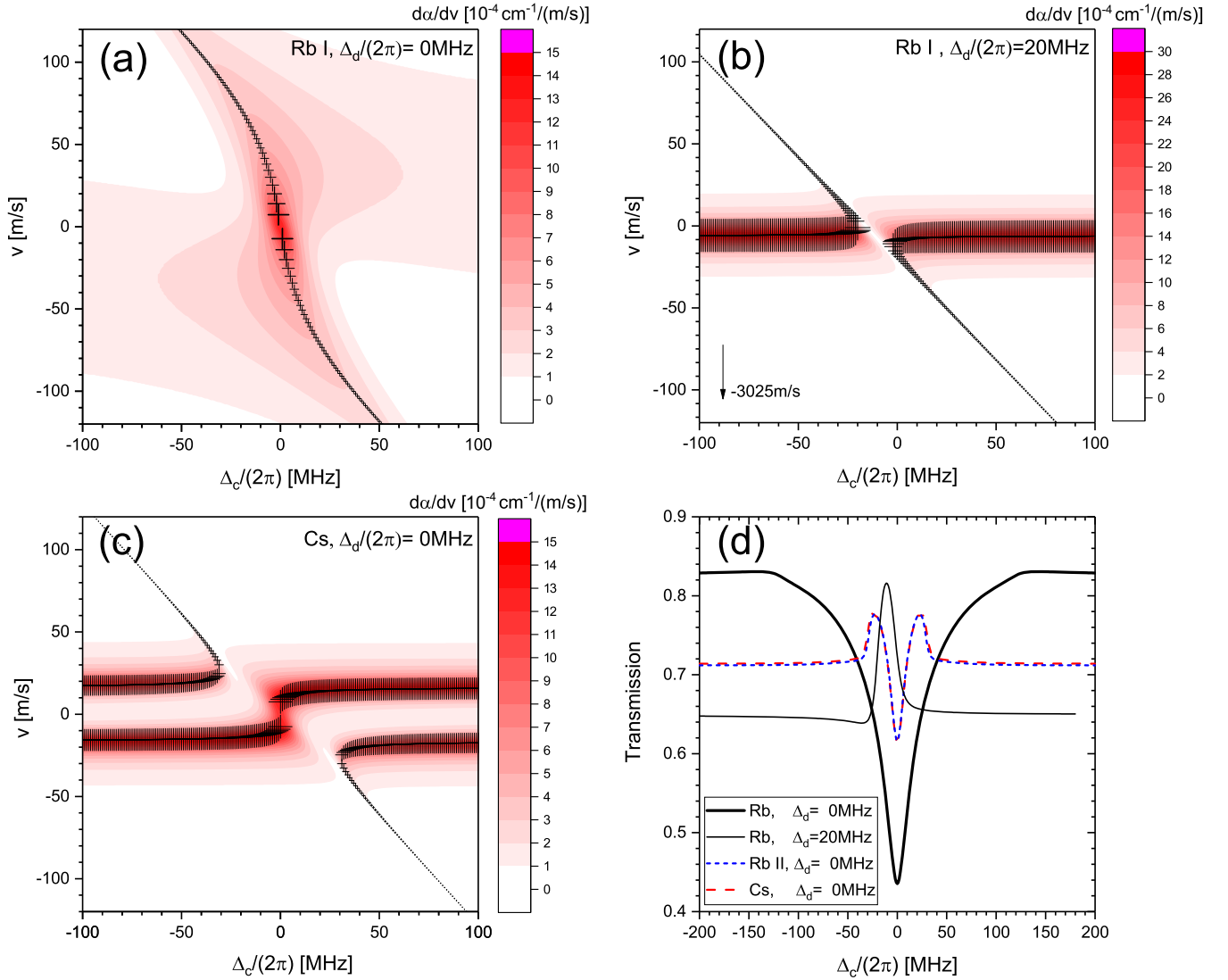


FIG. 3. (a–c) Velocity-specific absorption-coefficient maps, $[d\alpha/dv](\Delta_c, v)$, vs coupler detuning and velocity, displayed on linear color maps, for (+, −, −) configuration and the indicated values of the dressing-beam detuning, Δ_d , calculated with the complete numerical model from Sec. III. The probe detuning $\Delta_p = 0$, and Rabi frequencies are as in Fig. 2(b). The crosses and their diameters show positions and absorption strengths of dressed states derived from the analytical model explained in Sec. IV A 2, where atomic decay is neglected and the probe is assumed to be weak. Panels (a) and (b) correspond to EIA and EIT, respectively, for parameters as used in our rubidium experiment and cell temperature 300 K. For comparison, in (c) we show an absorption map and dressed-state positions and absorptions for EIA on the cesium cascade with wavelengths $\lambda_p = 852 \text{ nm}$, $\lambda_d = 1470 \text{ nm}$, and $\lambda_c = 790 \text{ nm}$. To allow for a comparison, atom density, velocity distribution $P(v)$, and Rabi frequencies are the same in (a)–(c). Panel (d) shows probe transmissions obtained from panels (a)–(c), and for the Rb cascade with wavelengths $\lambda_p = 780 \text{ nm}$, $\lambda_d = 1366 \text{ nm}$, and $\lambda_c = 740 \text{ nm}$ (labeled Rb II).

EIA signal. We further also explore the behavior at nonzero Δ_d .

Figure 2(a) shows experimental results for the (+, −, −) configuration and $\Delta_d/(2\pi) = -20, 0$, and $+20 \text{ MHz}$. The sub-THz field is turned off in this part of the paper. The examples shown in the figure illustrate our observation of strong EIA when Δ_d is close to zero and EIT when Δ_d is $\gtrsim 2\pi \times 5 \text{ MHz}$. Simulation results for this configuration are shown in Fig. 2(b). The simulated results show $\exp(-\alpha L)$, with cell length $L = 7.5 \text{ cm}$ and the absorption coefficient α computed for cell temperature 300 K using Eqs. (1)–(5). The Rabi frequencies in the simulation were $\Omega_p = 2\pi \times 10 \text{ MHz}$, $\Omega_d = 2\pi \times 25 \text{ MHz}$, and $\Omega_c = 2\pi \times 18 \text{ MHz}$; these values lead to

good agreement between simulated and experimental data. The EIA and EIT line shapes, linewidths, and signal depths agree well between the experimental and simulated data. [The experimental data show change in transmission on the same (arbitrary) scale for the different cases of Δ_d .] It is further seen, both in the experimental and in the simulated data, that the EIT linewidth at nonzero Δ_d is smaller than the width of the EIA dip at $\Delta_d = 0$. The $\approx 10\text{-MHz}$ shifts of the EIT peaks for $\Delta_d/(2\pi) = \pm 20 \text{ MHz}$ from $\Delta_c = 0$ are also reproduced.

2. Analytical model and comparison with the numerical model

To understand the results, it helps to first consider an analytical model for the case of weak probe ($\Omega_p \lesssim 2\pi \times 1 \text{ MHz}$),

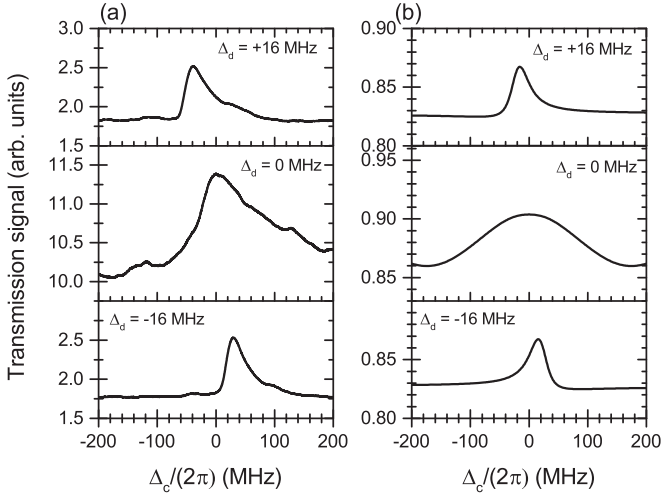


FIG. 4. (a) Experimental probe transmission signal vs Δ_c for the indicated values Δ_d , for laser beam directions in the (+, −, +) configuration. The transmission axes are on the same arbitrary scale, with zero corresponding to zero transmission. EIT is observed for all cases with $\Delta_d/(2\pi) = -16, 0, +16$ MHz. (b) Probe transmissions calculated with the model in Sec. III for cell temperature of 300 K, cell length $L = 7.5$ cm, and $\Omega_p = 2\pi \times 15$ MHz, $\Omega_d = 2\pi \times 30$ MHz, and $\Omega_c = 2\pi \times 18$ MHz.

large dressing and coupler Rabi frequencies, and no atomic decay. In this case, the strongly coupled three-level subspace $\{|e\rangle, |d\rangle, |r_1\rangle\}$ has, in a two-frequency dressed-atom picture and $\Delta_p = 0$, a Hamiltonian given by

$$H_{\text{sub}}(v) = \hbar \begin{pmatrix} vk_1 & \Omega_d/2 & 0 \\ \Omega_d/2 & -\Delta_d + vk_2 & \Omega_c/2 \\ 0 & \Omega_c/2 & -\Delta_d - \Delta_c + vk_3 \end{pmatrix}, \quad (6)$$

with $k_1 = k_p$, $k_2 = k_p - k_d$, and $k_3 = k_p - k_d \mp k_c$ for the (+, −, ∓) configurations. Since the microwave is off here, $|r_2\rangle$ is not coupled.

Absorption on the probe transition occurs for eigenstates with eigenvalue $s = 0$, i.e., we solve

$$H_{\text{sub}}(v) \begin{pmatrix} c_e \\ c_d \\ c_r \end{pmatrix} = s \begin{pmatrix} c_e \\ c_d \\ c_r \end{pmatrix} = \begin{pmatrix} 0 \\ 0 \\ 0 \end{pmatrix}, \quad (7)$$

where the c_i are the coefficients of a normalized eigenstate. Solving $\det[H_{\text{sub}}(v)] = 0$ amounts to finding the roots of a third-order polynomial in v , which has real solutions v_l with a counter l ranging from 1 to up to 3. The state coefficients $c_{i,l}$ then follow for each of the real roots, v_l . The strength of the probe absorption of atoms traveling at velocity v_l is proportional to $|c_{e,l}|^2$, and the net absorption summed over all roots is approximately proportional to $\sum_l P(v_l)|c_{e,l}|^2$. Here, we obtain the roots v_l as a function of Δ_c , for selected values of Δ_d , and plot them on the (Δ_c, v) plane. Using the Rabi frequencies Ω_d and Ω_c listed in Fig. 2, we plot the roots as crosses in Figs. 3(a) and 3(b); symbol diameter is proportional to $|c_{e,l}|$.

Our numerical model for the absorption, outlined in Sec. III, is more accurate because it accounts for the

level decays and probe saturation. Numerical solution of Eqs. (1)–(5) yields the velocity-specific absorption coefficient, i.e., absorption per velocity $[d\alpha/dv](\Delta_c, v)$. In Figs. 3(a)–3(c) the velocity-specific absorption maps are displayed as color-map backdrops. It is seen that the “ridge lines” of the velocity-specific absorption on the (Δ_c, v) plane closely track the analytical roots v_l derived from Eq. (6). Also, the values of $d\alpha/dv$, shown on the red color scale, are closely correlated with the $|c_{e,l}|$ values from Eq. (7). Therefore, the accurate, numerically solved model from Eqs. (1)–(5) and the analytical model from Eqs. (6) and (7) agree with each other quite well.

Both the analytical model from Eqs. (6) and (7) and the numerically solved Lindblad-equation model from Eqs. (1)–(5) are valuable. The former is useful because it lends itself to elucidate the underlying physics, while the latter is more accurate because it accounts for the level decays and probe saturation. Also, the numerical results for $d\alpha/dv$, integrated over v , yield the observable absorption coefficient, $\alpha(\Delta_c)$, which is required to quantitatively model our experimentally measured spectra. In the following we will use both the analytical model and the numerical solutions to interpret the various observed spectra.

3. Interpretation of results

We first discuss the case of EIA. In the middle curves in Fig. 2, the parameters are $\Delta_d = 0$, $k_2 < 0$, and $\Omega_c/\Omega_d < \sqrt{-k_3/k_1} = 1.266$. For this case it is found that Eq. (7) has only one real root, v_1 , at any Δ_c . Figure 3(a) shows $[d\alpha/dv](\Delta_c, v)$ and the root v_1 of Eq. (7) for this case. The root closely follows the “ridge line” of large $d\alpha/dv$ obtained in the exact calculation (dark-red regions on the color map). Also, $|c_{e,l}|$, indicated by symbol size, presents a good qualitative measure for the magnitude of $d\alpha/dv$ along the ridge line. Integrating the $d\alpha/dv$ data in Fig. 3(a) over v yields the thick solid curve in Fig. 3(d). In view of Fig. 3(a), it is apparent that EIA becomes particularly strong when the derivative of the root $dv_1/d\Delta_c$ at $\Delta_c = 0$ becomes large. In this case, absorption from a wide range of velocity classes in the vapor cell is accumulated at $\Delta_c \approx 0$, leading to particularly strong EIA. As previously discussed in [23], the EIA feature is deepest and narrowest when $\Omega_c/\Omega_d = \sqrt{-k_3/k_1} = 1.266$. This condition is equivalent to $[dv_1/d\Delta_c](\Delta_c = 0) \rightarrow \infty$.

For the Rb cascade studied in our experiment, EIA is enhanced even more because $k_2 \approx 0$ for this cascade. For $k_2 \approx 0$ the region of large $d\alpha/dv$ at $\Delta_c \approx 0$ extends over a particularly wide range in velocity [see Fig. 3(a)], leading to a large integral $[\int [d\alpha/dv]dv](\Delta_c)$, as evident in the thick solid curve in Fig. 3(d). In contrast, for large and positive k_2 , the case of [23], one finds that Eq. (7) has three roots in most Δ_c domains and that the region of large $d\alpha/dv$ at $\Delta_c = 0$ is limited to $|v| \lesssim \Omega_d/(2\sqrt{k_1 k_2})$. This is visualized in Fig. 3(c), which is for the Cs transitions chosen in [23]. There, for $\Omega_d = 2\pi \times 25$ MHz the region of large $d\alpha/dv$ is capped at $|v| \lesssim \Omega_d/(2\sqrt{k_1 k_2}) = 16.5$ m/s, leading to a comparatively small EIA effect at $\Delta_c \approx 0$. The three transmission curves plotted in Fig. 3(d) for $\Delta_d = 0$ demonstrate that the Rb case with $\lambda_p = 780$ nm and $\lambda_d = 776$ nm has, indeed, by far the strongest EIA.

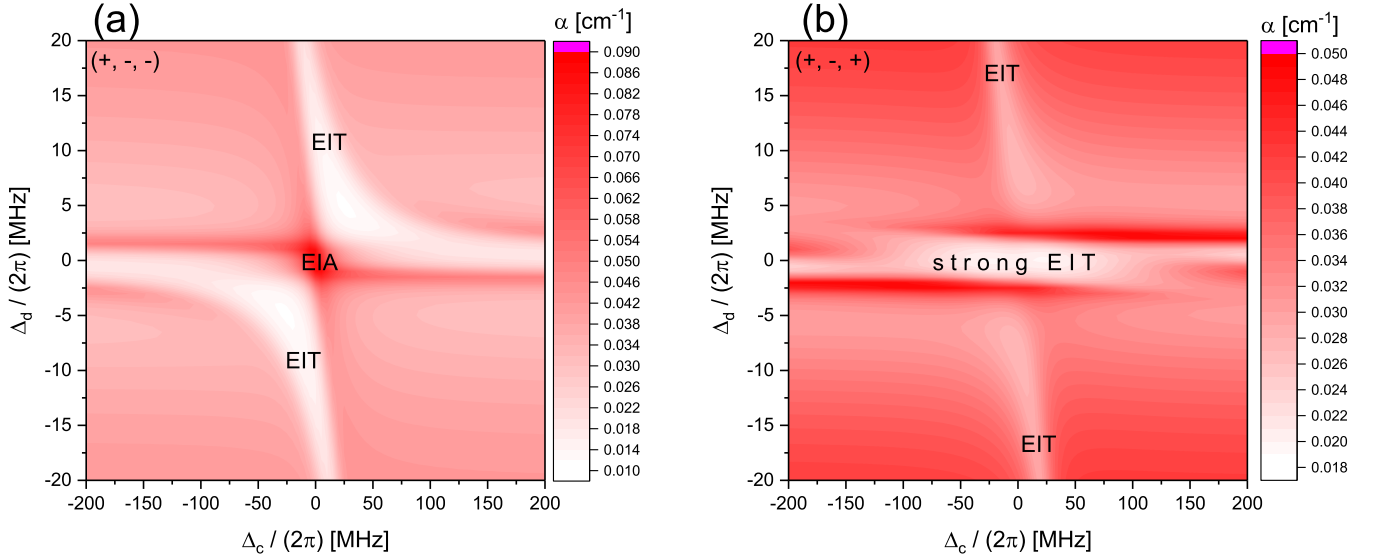


FIG. 5. Absorption coefficient, calculated with the model in Sec. III, for Rb three-photon EIT and EIA for the level scheme shown in Fig. 1 (without microwave) vs coupler (horizontal) and dressing detuning (vertical axis) for the $(+, -, -)$ (a) and the $(+, -, +)$ (b) beam-direction configurations. To allow for a comparison, in both (a) and (b) we have used the same Rabi frequencies, $\Omega_p = 2\pi \times 10$ MHz, $\Omega_d = 2\pi \times 25$ MHz, and $\Omega_c = 2\pi \times 18$ MHz.

For comparison, in Fig. 3(d) we additionally show the EIA curve for the $5S_{1/2} \leftrightarrow 5P_{3/2} \leftrightarrow 6S_{1/2} \leftrightarrow nP_J$ cascade in Rb, which has wavelengths $\lambda_p = 780$ nm, $\lambda_d = 1366$ nm, $\lambda_c = 740$ nm, and $k_2 \gg 0$. It is seen that this case exhibits relatively weak EIA, similar to that of the Cs cascade studied in [23].

We now briefly discuss the case of EIT for the off-resonant dressing beam and then consider the context between EIA and EIT. In Fig. 3(b) we show the roots v_l of Eq. (7) and the exact solution for $d\alpha/dv$ for the case $\Delta_d = 2\pi \times 20$ MHz (top curves in Fig. 2). Except for $\Delta_c \sim 0$, there are three roots. One root is not shown because it is near $v = -3025$ m/s, where there are no atoms. The other two roots form a comparatively narrow anticrossing that results in correspondingly narrow EIT transmission signals [Fig. 2 top and bottom panels and thin black curve in Fig. 3(d)].

The difference in behavior seen at zero and at substantially non-zero Δ_d (strong, wider EIA vs somewhat less strong, narrower EIT) corresponds to different limits of the dressed states formed by the dressing transition. The velocity roots that correspond to the two dressed states at large Δ_c (or, with the coupler turned off) are given by $v_{\pm} = \frac{\Delta_d}{2k_2} \pm \sqrt{(\frac{\Delta_d}{2k_2})^2 + \frac{\Omega_d^2}{4k_1k_2}}$. For $\Delta_d = 0$ and $k_2 > 0$, resonant coupling results in a pair of symmetric and antisymmetric Autler-Townes (AT) split states at $v_{\pm} = \pm \frac{\Omega_d}{2\sqrt{k_1k_2}}$ that both have 50% probability in $|e\rangle$, leading to two equally strong horizontal absorption bands, as seen in Fig. 3(c). The width of the EIA feature near $\Delta_c = 0$ scales with Ω_c [see Fig. 3(c) and the cases of $\Delta_d = 0$ in Fig. 3(d)]. Note that in Fig. 3(a) the horizontal absorption bands are absent because $k_2 < 0$. On the other hand, for large Δ_d the two AT states are highly asymmetric. In that case, the dressing and coupler beams drive a two-photon transition that has intermediate detuning Δ_d from the $|d\rangle$ level and two-photon Rabi frequency $\Omega_d \Omega_c / (2\Delta_d)$. This leads to narrow EIT lines at large Δ_d , with widths on the order of $\Omega_d \Omega_c / (2\Delta_d)$ [see Fig. 3(b) and the case of $\Delta_d = 2\pi \times 20$ MHz in Fig. 3(d)].

B. $(+, -, +)$ configuration and comparison

Figure 4(a) shows experimental results when the laser beams are in $(+, -, +)$ configuration. We obtain strong EIT signals when Δ_d is close to zero and weak EIT signals when $\Delta_d = \pm 2\pi \times 16$ MHz. The results show reasonable agreement with the simulation in Fig. 4(b). In both experiment and simulation it is seen that the $\Delta_d = 0$ case exhibits wide, massive EIT over the entire range of Δ_c , with a broad peak around $\Delta_c = 0$ and narrower, less high and asymmetric EIT peaks in the detuned- Δ_d cases. In the detuned- Δ_d cases, the EIT peaks are shifted from $\Delta_c = 0$, both in experimental and in simulated results. Measured and simulated spectra deviate from each other in that in all cases the experimental EIT peaks are lopsided to the right. This may be attributable to slight elliptical polarizations and optical pumping of the atoms within the interaction volume. Such effects are not covered by our model because it neglects magnetic substructure.

In Fig. 5 we present an overview calculation to compare the EIT and EIA effects between the $(+, -, \mp)$ configurations. The absorption coefficient is plotted vs coupler-laser detuning, Δ_c (horizontal axis), for a range of dressing-beam detunings, Δ_d (vertical axis). All phenomena explained above are reproduced. Noting the difference in color-scale range, it is reaffirmed that the $(+, -, +)$ case generally exhibits much stronger EIT than the $(+, -, -)$ case, across all frequency detunings.

In terms of linewidth and signal height and depth, the Rydberg-EIT and -EIA features in the $(+, -, \mp)$ configurations can be ranked in usability for Rydberg-state spectroscopy in the following descending order: (1) $(+, -, -)$ -EIT, (2) $(+, -, -)$ -EIA, (3) $(+, -, +)$ -EIT for $\Delta_d \neq 0$, and (4) $(+, -, +)$ -EIT for $\Delta_d = 0$.

In the next section we calibrate a 100-GHz transmission system using EIT and EIA in the $(+, -, -)$ configuration, the

measurement methods that rank the highest in our comparison.

V. MICROWAVE MEASUREMENTS

Rydberg spectroscopy presents an excellent tool for microwave [5] and sub-THz [25] metrology. Using three-photon Rydberg-EIT and -EIA with red and infrared laser diodes may present an advantage over the more widely used two-photon Rydberg-EIT due to reduced cost and the fact that red and infrared light may cause less photoelectric effect and ionization within the vapor cells, potentially reducing the effects of dc electric fields on the quality of the Rydberg spectra. Here we use microwave-field-induced AT splitting on the $\text{Rb } 28F_{7/2} \leftrightarrow 29D_{5/2}$ resonance to measure a microwave field.

The $28F_{7/2} \leftrightarrow 29D_{5/2}$ transition has a large radial electric dipole moment matrix element of 1047 ea_0 and an average angular matrix element for the relevant π -polarized transitions ($m = 1/2$ and $3/2$) of 0.47 . The effective electric dipole moment \bar{d}_z is the product of the radial and averaged angular matrix elements. The microwave field, E_{rf} , follows from

$$E_{\text{rf}} \approx \frac{\hbar \Delta_{\text{AT}}}{\bar{d}_z}, \quad (8)$$

with AT splitting Δ_{AT} and $\bar{d}_z = 492 \text{ ea}_0$. The large value of \bar{d}_z makes the measurement method very sensitive to the microwave field. We set the microwave generator (Keysight N5183A MXG) at a frequency of 25.1582 GHz . The field is frequency quadrupled using an active frequency multiplier (Norden N14-4680) to reach the microwave frequency of 100.633 GHz , which is on resonance with the $28F_{7/2} \rightarrow 29D_{5/2}$ transition. The AT splitting observed in three-photon Rydberg-EIT and -EIA approximates the microwave Rabi frequency, Ω_{rf} , which in turn reveals the microwave electric field according to Eq. (8) [2,26,27].

In Fig. 6 we present measurements for both EIA (left) and EIT (middle) in the $(+, -, -)$ configuration, as well as the derived AT splittings (right), for the indicated power levels of the 25-GHz signal generator. It is evident that the EIT signals have a narrower linewidth, allowing one to resolve the AT peaks at a lower microwave field than in the EIA case. In the present case, the AT-splitting data allow us to perform an absolute calibration of the 100-GHz microwave electric field at the location of the vapor cell relative to the utilized microwave horn (Chendu LB-10-15). The AT splittings [left axis in Fig. 6(c)] and Eq. (8) yield the rf electric field (right axis). The data in Fig. 6(c) show that below saturation the quadrupler power scales as the ninth power of the signal-generator power, highlighting the fact that the quadrupler is a highly nonlinear device.

The saturation rf electric field of the quadrupler at the atom location is about 11 V/m , as seen in Fig. 6(c). Using the standard gain from the horn manufacturer's data sheet, 18.7 dBi , and the chosen distance between the horn and the cell, 28 cm (which is in the far field), the maximum radiated power from the quadrupler is estimated at 2 mW . The quadrupler data sheet specifies 1 mW . The slight elevation of our power measurement may be due to constructive standing-wave interference of the 100-GHz field within the

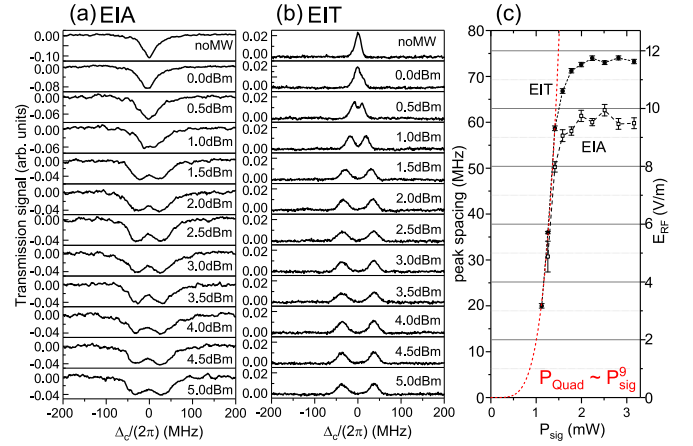


FIG. 6. (a) A series of measured EIA spectra in $(+, -, -)$ configuration with $\Delta_d = 0$ and a microwave field of 100.633 GHz driving the $28F_{7/2} \leftrightarrow 29D_{5/2}$ transition. The probe field is horizontally polarized and all other fields are vertically polarized. The spectra are labeled by the power P_{sig} the signal generator supplies to the frequency quadrupler. The vertical scales show change in transmission relative to the case of no coupler light. (b) Same for EIT in $(+, -, -)$ configuration with $\Delta_d = -2\pi \times 80 \text{ MHz}$. (c) Autler-Townes splittings (left axis) from panels (a) and (b) and derived microwave electric fields (right axis) vs P_{sig} . An allometric fit to the EIT data shows that in the nonsaturated regime the quadrupler power scales with the ninth power of P_{sig} .

cell [4,28–30], which would increase the measured output power of the quadrupler, and/or to a conservative quadrupler specification (i.e., the quadrupler might perform slightly better than specified). The change in laser beam paths between the EIA and EIT sets of data shown in Fig. 6 may have caused a slight variation in standing-wave effects, which could explain the difference in saturation electric fields between the EIT and EIA measurements of the rf electric field.

Finally, we have modeled the rf spectra in Fig. 6 along the lines of Eqs. (1)–(5). The results, shown in Fig. 7, are in good agreement with the measured spectra. It is, in particular, confirmed that the EIT signal at large dressing-beam detuning Δ_d allows one to resolve smaller AT splittings than the EIA signal, due to the smaller width of the EIT peaks.

VI. DISCUSSION

Calculated and measured results in Secs. IV and V generally agree very well. We attribute this to a variety of factors. First, there are no low-lying uncoupled metastable states the atoms could get optically pumped into. Further, because the atoms in the room-temperature vapor cell move at speeds on the order of 200 m/s through laser beams with diameters of about $100 \mu\text{m}$, the atom-field interaction times are quite short ($\lesssim 1 \mu\text{s}$). This negates significant effects due to natural decay and blackbody-radiation-driven decay of the Rydberg atoms into uncoupled metastable Rydberg levels outside of the closed five-level system assumed in the calculation. Next, while collision-induced Rydberg-level dephasing is included as an option in our model, this feature is not needed in order to reproduce the experimental data to within the experimental

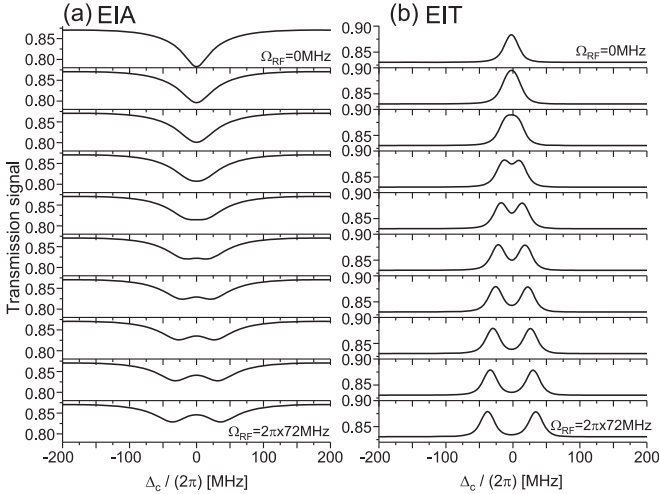


FIG. 7. Calculated EIA (a) and EIT (b) transmission spectra with the rf field turned on, for $\Delta_d = 0$ and $-2\pi \times 80$ MHz, respectively. The laser beams are in (+, -, -) configuration, and the optical Rabi frequencies are $\Omega_p = 2\pi \times 20$ MHz, $\Omega_d = 2\pi \times 25$ MHz, and $\Omega_c = 2\pi \times 18$ MHz. The rf Rabi frequency ranges from 0 (top) to $2\pi \times 72$ MHz (top), varied in equidistant steps.

confidence levels. Finally, another reason for the success of the five-level model is the absence of significant magnetic fields. Fields exceeding ≈ 1 G would introduce Zeeman splittings and complex optical-pumping dynamics [31] that cannot be captured in a five-level model.

Another effect of the short duration of the atom-field interaction in the cell ($\lesssim 1 \mu\text{s}$) may be interaction-time broadening. In Ref. [23] interaction-time broadening was modeled by adding level dephasing to the Rydberg state. We have run our simulation for Rydberg-level dephasings of up to $2\pi \times 6$ MHz, as well as for cases where all excited levels were assigned a dephasing of up to $2\pi \times 3$ MHz. Level dephasings on that order are compatible with the frequency bandwidth of the atom-field interactions in our setup. The results indicate no effects that would be observable in our experiment. More simulation details are shown in the Supplemental Material [32]. Level dephasing can also be used to model the effects of energy shifts caused by non-state-changing collisions, for which there is no evidence in our paper.

Level dephasing does not capture the physics of coherent transients. Therefore we have modeled the interaction-time broadening by integrating the Lindblad equation over times on the order of $1 \mu\text{s}$. The laser pulses, turned on at time $t = 0$, generate transients in the coherences and populations of the density operator. As before, the time-dependent density operators obtained from the simulation are averaged over the velocity distribution of the atoms in the cell. The absorption coefficient and the EIT and EIA signals that follow from the density operator become functions of time. In the Supplemental Material [32] we show that, while the transients are quite

substantial, they damp out over times $\lesssim 1 \mu\text{s}$. We also see that the absorption signals averaged over the duration of a $1\text{-}\mu\text{s}$ drive pulse are not significantly different from steady-state results. Our findings with regard to the time scale on which the steady state is reached agree with previous findings, according to which EIT typically is established over time scales on the order of the intermediate-state lifetimes [33] (which range from 30 to 300 ns in our case). Therefore, transit-time broadening is not expected to play a role in our experimental spectra. Additional discussion on this topic as well as a movie that illustrates the time evolution of the transients are provided in the Supplemental Material [32].

In Fig. 2(a), top curve, and in Fig. 4(a), middle curve, we see weak side structures at about 100 MHz from the center. We could not explain these structures with level schemes that involve other hyperfine states of the $5P_{3/2}$ or $5D_{5/2}$ levels, or the $28F_{5/2}$ fine-structure level. We therefore believe that the side structures may be due to an experimental imperfection, such as beam reflections inside the vapor cell.

VII. CONCLUSION

We have performed a comprehensive experimental and theoretical study of three-photon Rydberg-EIA and -EIT systems in an atomic vapor cell. Physical interpretations have been provided that elucidate the underlying physics. Figure 6 demonstrates that three-photon Rydberg-EIT, with low-cost all-infrared laser diode systems, may be valuable for absolute calibration of microwave frequency instrumentation. This could be particularly useful in the sub-THz and THz frequency regimes, where detectors can be inaccurate or may be unavailable. In future work it is desirable to account for optical-pumping effects, as well as for line splittings in complex rf spectra (for instance, spectra obtained in stronger rf fields or with more highly excited Rydberg levels). The large Hilbert spaces in such extended Rydberg-EIT and -EIA systems can be modeled efficiently using quantum Monte Carlo wave-function methods [31,34] and Floquet methods [35,36], respectively. While, with our present time resolution, transient signals could not be observed, higher-speed photodiodes should enable direct observation of EIT and EIA transients in pulsed laser fields. Finally, it is noted that three-photon EIA and EIT allow, in principle, for perfect compensation of Doppler effects using noncollinear beams in a star-beam configuration, with beam angles chosen such that Doppler shifts cancel. This approach may be viable in microfabricated cells with cell diameters on the order of the laser beam diameters.

ACKNOWLEDGMENTS

This work was supported by the NSF (Grants No. PHY-1806809 and No. PHY-1707377). D.A.A. acknowledges support by Rydberg Technologies, Inc.

[1] T. Gallagher, *Rydberg Atoms* (Cambridge University, Cambridge, England, 2005), Vol. 3.

[2] J. A. Sedlacek, A. Schwettmann, H. Kübler, R. Löw, T. Pfau, and J. P. Shaffer, *Nat. Phys.* **8**, 819 (2012).

- [3] J. A. Gordon, C. L. Holloway, A. Schwarzkopf, D. A. Anderson, S. Miller, N. Thaicharoen, and G. Raithel, *Appl. Phys. Lett.* **105**, 024104 (2014).
- [4] C. L. Holloway, J. A. Gordon, A. Schwarzkopf, D. A. Anderson, S. A. Miller, N. Thaicharoen, and G. Raithel, *Appl. Phys. Lett.* **104**, 244102 (2014).
- [5] C. Holloway, J. Gordon, S. Jefferts, A. Schwarzkopf, D. Anderson, S. Miller, N. Thaicharoen, and G. Raithel, *IEEE Trans. Antennas Propag.* **62**, 6169 (2014).
- [6] S. A. Miller, D. A. Anderson, and G. Raithel, *New J. Phys.* **18**, 053017 (2016).
- [7] A. Horsley and P. Treutlein, *Appl. Phys. Lett.* **108**, 211102 (2016).
- [8] H. M. Kwak, T. Jeong, Y.-S. Lee, and H. S. Moon, *Opt. Commun.* **380**, 168 (2016).
- [9] D. A. Anderson and G. Raithel, *Appl. Phys. Lett.* **111**, 053504 (2017).
- [10] D. A. Anderson, R. E. Sapiro, and G. Raithel, *arXiv:1808.08589*.
- [11] A. B. Deb and N. Kjærgaard, *Appl. Phys. Lett.* **112**, 211106 (2018).
- [12] D. H. Meyer, K. C. Cox, F. K. Fatemi, and P. D. Kunz, *Appl. Phys. Lett.* **112**, 211108 (2018).
- [13] D. Anderson, E. Paradis, and G. Raithel, *Appl. Phys. Lett.* **113**, 073501 (2018).
- [14] A. K. Mohapatra, T. R. Jackson, and C. S. Adams, *Phys. Rev. Lett.* **98**, 113003 (2007).
- [15] S. Mauger, J. Millen, and M. Jones, *J. Phys. B* **40**, F319 (2007).
- [16] K.-J. Boller, A. Imamoglu, and S. E. Harris, *Phys. Rev. Lett.* **66**, 2593 (1991).
- [17] M. Fleischhauer, A. Imamoglu, and J. P. Marangos, *Rev. Mod. Phys.* **77**, 633 (2005).
- [18] K. Weatherill, J. Pritchard, R. Abel, M. Bason, A. Mohapatra, and C. Adams, *J. Phys. B* **41**, 201002 (2008).
- [19] J. D. Pritchard, D. Maxwell, A. Gauguier, K. J. Weatherill, M. P. A. Jones, and C. S. Adams, *Phys. Rev. Lett.* **105**, 193603 (2010).
- [20] D. Petrosyan, J. Otterbach, and M. Fleischhauer, *Phys. Rev. Lett.* **107**, 213601 (2011).
- [21] C. Ates, S. Sevincli, and T. Pohl, *Phys. Rev. A* **83**, 041802(R) (2011).
- [22] L. A. M. Johnson, H. O. Majeed, B. Sanguinetti, T. Becker, and B. T. H. Varcoe, *New J. Phys.* **12**, 063028 (2010).
- [23] C. Carr, M. Tanasittikosol, A. Sargsyan, D. Sarkisyan, C. S. Adams, and K. J. Weatherill, *Opt. Lett.* **37**, 3858 (2012).
- [24] J. Shaffer and H. Kübler, in *Proceedings of SPIE Photonics Europe*, 2018 (unpublished), Vol. 10674, p. 106740C.
- [25] D. A. Anderson, E. Paradis, G. Raithel, R. E. Sapiro, and C. L. Holloway, in *Proceedings of the 2018 11th Global Symposium on Millimeter Waves*, 2018 (unpublished), pp. 1–3.
- [26] C. L. Holloway, M. T. Simons, J. A. Gordon, A. Dienstfrey, D. A. Anderson, and G. Raithel, *J. Appl. Phys.* **121**, 233106 (2017).
- [27] H. Kübler, J. Keaveney, C. Lui, J. Ramirez-Serrano, H. Amarloo, J. Erskine, G. Gillet, and J. P. Shaffer, in *Proceedings of SPIE 10934, Optical, Opto-Atomic, and Entanglement-Enhanced Precision Metrology*, 2019 (unpublished), Vol. 10934.
- [28] H. Q. Fan, S. Kumar, R. Daschner, H. Kübler, and J. P. Shaffer, *Opt. Lett.* **39**, 3030 (2014).
- [29] H. Fan, S. Kumar, J. Sheng, J. P. Shaffer, C. L. Holloway, and J. A. Gordon, *Phys. Rev. Applied* **4**, 044015 (2015).
- [30] C. Holloway, M. Simons, J. Gordon, P. Wilson, C. Cooke, D. Anderson, and G. Raithel, *IEEE Trans. Electromagn. Compat.* **59**, 717 (2017).
- [31] L. Zhang, S. Bao, H. Zhang, G. Raithel, J. Zhao, L. Xiao, and S. Jia, *Opt. Express* **26**, 29931 (2018).
- [32] See Supplemental Material at <http://link.aps.org/supplemental/10.1103/PhysRevA.100.063427> for calculation results.
- [33] M. O. Scully and M. S. Zubairy, *Quantum Optics* (Cambridge University, Cambridge, England, 1997), p. 225ff.
- [34] Y. Xue, L. Hao, Y. Jiao, X. Han, S. Bai, J. Zhao, and G. Raithel, *Phys. Rev. A* **99**, 053426 (2019).
- [35] D. A. Anderson, A. Schwarzkopf, S. A. Miller, N. Thaicharoen, G. Raithel, J. A. Gordon, and C. L. Holloway, *Phys. Rev. A* **90**, 043419 (2014).
- [36] D. A. Anderson, S. A. Miller, G. Raithel, J. A. Gordon, M. L. Butler, and C. L. Holloway, *Phys. Rev. Applied* **5**, 034003 (2016).